Journal Name

ARTICLE

Optimized silk fibroin piezoresistive nanocomposites for pressure sensing applications based on natural polymers

Received 00th January 20xx,
Accepted 00th January 20xx

DOI: 10.1039/x0xx00000x

www.rsc.org/

Ander Reizabal,[a,b] Sérgio Gonçalves, [c,d,e] Ricardo Brito-Pereira, [c] Pedro Costa, [c,f] Carlos M. Costa, *[c,g] Leyre Pérez-Álvarez, [a,b] Jose Luis Vilas-Vilela [a,b] and Senentxu Lanceros-Méndez *[a,h]

Environmental issues promote the development of sensors based on natural polymers that are becoming an area of increasing interest. Piezoresistive sensors based on silk fibroin with carbon nanotubes (CNT) as fillers were produced by solvent-casting in order to tune their electrical conductivity and electromechanical response. It is shown that the carbonaceous fillers are well dispersed in the polymer matrix and the thermal and mechanical properties are independent of the CNT content. On the other hand, the inclusion of CNT reduces the β-sheet content of silk fibroin and the electrical properties of the composite strongly depend on the filler content, being the percolation threshold around 1wt.% of CNT. The piezoresistive response demonstrates good reproducibility during cyclic loading without hysteresis with a piezoresistive sensitivity of ~ 4 MPa^{-1}, regardless of the CNT content. Overall, the results confirm that polymer composites based on natural polymers allow excellent piezoresistive response, also demonstrated by the implementation and testing of a pressure sensor with the corresponding readout electronics. Thus, it is shown that natural polymer such as silk fibroin will allow the development of a new generation of multifunctional force and deformation sensors.

Introduction

Remarkable achievements have been obtained in polymer composites allowing to improve their thermal, mechanical and electrical properties for applications in areas such as construction, electronics, consumer products, sensors and actuators, biological applications, and energy, among others [1-3]. The main recent focus for those materials is to obtain high performance composites based on natural polymers and biopolymers, in order to reduce the use of polymers obtained from crude oil, while maintaining the functional performance [4]. The prefix 'bio' in biopolymers means that they are produced from biological sources, including biomass –e.g. agro-polymers - as well as by microbial production or other living organisms [5, 6]. Starches, pectins, chitosan / chitin, collagen / gelatin, poly (hydroxybutyrate) (PHB) poly (lactic acid) (PLA), or silk fibroin (SF) are some of the more reported biopolymers in the literature [5].

In particular, silk fibroin, mainly obtained from the *Bombyx mori* cocoon, deserves special attention within natural polymers due to its non-toxicity, excellent mechanical, thermal and electrical properties (e.g. piezoelectric response), biocompatibility and controllable biodegradability, being obtained in a wide range of morphologies and applied in a wide range of applications ranging from textile to healthcare sectors [7, 8].

Silk fibroin is composed by glycine (45%), alanine (30%), and serine (12%) in a roughly 3: 2: 1 ratio and dominated by $[Gly-Ala-Gly-Ala-Gly-Ser]_n$ sequences with β-sheet crystallites and amorphous domains [9, 10].

A wide variety of structures and morphologies can be obtained from silk fibroin [11], its functional characteristics and processability supporting the selection of silk fibroin [12] for a wide range of applications in the areas of biomedicine [13], optical, photonic and electronics [14, 15].

Piezoresistive sensors based on natural polymers are useful for force and deformation measurements, and present a high potential in the scope of Industry 4.0 and Internet of Things

[a.] BCMaterials, Basque Center for Materials, Applications and Nanostructures, UPV/EHU Science Park, 48940 Leioa, Spain, email: senentxu.lanceros@bcmaterials.net
[b.] Macromolecular Chemistry Research Group (LABQUIMAC). Dept. of Physical Chemistry. Faculty of Science and Technology, University of the Basque Country (UPV/EHU), Spain.
[c.] Center of Physics, University of Minho, 4710-058 Braga, Portugal, email: cmscosta@fisica.uminho.pt.
[d.] Centro ALGORITMI, University of Minho, Campus de Azurém, 4800-058 Guimarães, Portugal.
[e.] EngageLab, University of Minho, 4810-453 Guimarães, Portugal.
[f.] Institute for Polymers and Composites IPC/i3N, University of Minho, 4800-058 Guimarães, Portugal.
[g.] Center of Chemistry, University of Minho, 4710-058 Braga, Portugal.
[h.] Ikerbasque, Basque Foundation for Science, 48013 Bilbao, Spain.

paradigms, which increasingly demand a large variety of environmental friendlier sensors [16, 17].

There are different types of piezoresistive sensors, however, taking into account their flexibility, easy processability and integrability, the most outstanding are piezoresistive polymer based composites [18, 19]. Those composites are composed by a polymer matrix and conductive fillers, being the most used ones carbonaceous fillers such as carbon black [20], carbon nanofibers (CNF) [21], carbon nanotubes (CNT) [22] and graphene [23]. The final properties of the composites (electrical, mechanical, thermal and electromechanical) are determined by filler type, content and aspect ratio [24]. Polymer matrices typically used for piezoresistive composites include from thermoplastics [25] to elastomers [26] but the use of natural polymers is scarce in the literature.

Some works have been reported on polymer composites based on silk fibroin and carbon nanotubes (CNT) for biomedical application [27, 28] and enzymatic biofuel cells [29]. The silk fibroin/CNT composites were obtained by the template method leading to a conductive composite that was used are permissive neuronal interfaces allowing adhesion and differentiation of dorsal root ganglion neuronal cells (DRG) in vitro [27].

In addition, electrospinning has been used to prepare silk fibroin/CNT composites using formic acid as a solvent. It is observed that carbon nanotubes are incorporated along the nanofibers, leading to enhanced mechanical properties with the incorporation of small amount of CNTs [28].

Further, silk fibroin cryogels with carbon nanotubes were fabricated by a sol-gel process followed by freeze-drying where the carbon nanotubes were incorporated within the porous three-dimensional silk fibroin network structure, leading to a change in the crystal structure of silk fibroin [30].

In order to explore and expand the applicability of silk fibroin, this work proposes silk fibroin nanocomposites based on carbon nanotubes for the fabrication of piezoresistive sensors. The aim of this work is to evaluate the morphological, thermal, mechanical and electrical properties of silk fibroin films with different amounts of carbon nanotubes, paying particular attention to the electrical and electromechanical properties in order to develop multifunctional materials for sensors and actuators applications.

Experimental

Materials

Bombyx mori cocoons were supplied by APPACDM from Castelo Branco (Portugal). Carbon nanotubes (CNTs) were provided by Nanocyl (reference NC7000, purity of 90%, 1.5 µm length and an outer mean diameter of 9.5 nm).

Composite film preparation

Bombyx mori cocoons were cut into small pieces and degummed by boiling them for 30 min in a 0.02 M Na_2CO_3 solution. For each 1 g of silk, 40 ml of aqueous Na_2CO_3 solution were used. After that, the fibers were rinsed several times with distilled water, squeezed out to remove the excess water, and finally dried overnight in a fume hood. Once fibers were totally dried, they were dissolved in a formic acid/$CaCl_2$ (FA) 0.2M solution with 10 ml FA per gram of SF. After centrifugation to remove insoluble residues, the silk solution was placed in an airing chamber to allow fast evaporation of formic acid within 24h. $CaCl_2$ was removed by progressive washing with distilled water until the solution showed a constant conductivity. Finally, purified SF was dried overnight in a fume hood.

For SF/CNT composites preparation, solutions were prepared in formic acid with different amounts of CNT (0.25, 0.5, 0.75, 1, 3, 6 wt.%, related to SF). Fillers were initially added to formic acid and mixed by ultrasonication bath, during 3h, to ensure good dispersion and to prevent nanotubes agglomeration. Afterwards, SF (8% (wt.%)) was added. Once proteins were completely dissolved by magnetic stirring, solution was treated in a sonication needle during 5 minutes with 30% of amplitude, 7 seconds of treatment and 3 seconds of landing, to ensure the correct dispersion of the fillers. The obtained SF/CNT mixture was cast overnight in polypropylene Petri dishes and dried to remove all the formic acid and promote β-sheets crystals formation. The processing steps and corresponding sequence are illustrated in Figure 1.

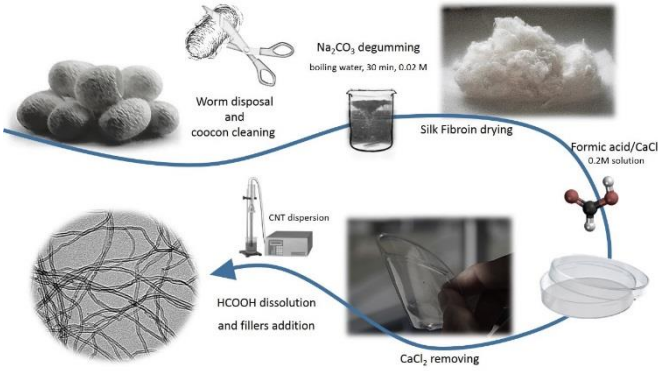

Figure 1. Main experimental steps for the processing of SF/CNT composites.

Characterization techniques

The morphology of the samples and the dispersion of CNT were examined with a scanning electron microscope (SEM, NanoSEM - FEI Nova 200 (FEG/SEM)) with an accelerating voltage of 15 kV. The films were previously deposited with a conductive gold layer by sputtering with a Polaron SC502 apparatus.

The structure of the silk fibroin films and possible interaction between the CNT and the polymer matrix were evaluated by Fourier Transformed Infrared Spectroscopy (FTIR) performed at room temperature with a Jasco FT/IR-4100 system. FTIR spectra were collected in the ATR mode from 4000 to 600 cm^{-1} after 64 scans with a resolution of 4 cm^{-1}.

In order to determine the relative content of the secondary structures present in each sample, the deconvolution of band in the spectral region corresponding to Amide I was carried out with the OriginPro 8.1 software (OriginLab, Northampton).

The thermal behavior of the samples was determined by Differential Scanning Calorimetry (DSC) and Thermo Gravimetric Analysis (TGA).

DSC was performed with a Mettler Toledo DSC 822e apparatus with sample robot between 25 and 350 °C at 10 °C min^{-1} under nitrogen purge (50 mL min^{-1}) in 40 µL aluminium cans with perforated lids. TGA was carried out using a TGA/SDTA 851e Metter Toledo apparatus under a flow rate of 50 mL.min^{-1} operating between 25 to 800 °C at 10 °C min^{-1}.

Dynamic mechanical analysis (DMA) was performed with a Metter Toledo DMA1 apparatus in the tensile mode. The storage modulus and loss tangent were measured as a function of temperature at a frequency of 1 Hz from 0 °C to 280 °C and a heating rate of 3 °C/min. The measurements were performed in samples with typical dimensions of 10 × 4 × 0.050 mm.

Dielectric measurements were performed using a Quadtech 1920 LCR precision meter. The capacity and the dielectric losses (tan δ) were obtained at room temperature in the frequency range of 20 Hz to 1 MHz with an applied voltage of 0.5 V. Circular gold electrodes of 5 mm diameter were deposited on both sides of each sample with a Polaron SC502 sputter system. The error associated with the dielectric measurements is ~1%, mainly due to the determination of the geometrical parameters with as Mitutoyo micrometer.

The real part of the dielectric function (ε') and the a.c. electrical conductivity (σ') were determined through the following equations:

$$\varepsilon' = \frac{C.d}{\varepsilon_0.A} \quad (1)$$

and

$$\sigma' = \varepsilon_0 \omega \varepsilon' tan\delta \quad (2)$$

Where C is the capacitance (F), ε_o is the permittivity of vacuum (8.85×10^{-12} F m^{-1}), A is the electrode area (m^2), d is the thickness of samples (m) and $\omega = 2\pi\nu$ is the angular frequency.

The D.C. electrical conductivity of the samples was obtained by a 2-wire method with an applied voltage between ±10 V and measuring the current through a Keithley 487 picoammeter/voltage source. Volume resistivity was measured at room temperature in samples with circular contacts of 5 mm diameter and the resistivity of the samples (ρ *in S/m*) was obtained from the slope of the I–V curves and calculated by:

$$\rho = \frac{R.A}{d} \quad (3)$$

where R is the resistance of the sample, d its thickness and A is the electrode area.

Electro-mechanical tests were performed by measuring the volume electrical resistance (Agilent 34401A multimeter) in real time using the two-probe method while the samples were subjected to the cyclic compression load with a Shimadzu AG-IS with load cell of 500 N (Instron 5544) at 2 mm/min.

The electro-mechanical test under compressive were evaluated by the pressure sensitivity (PS) through the following equation [31]:

$$PS = \frac{\Delta R/R_0}{P} \quad (4)$$

where R_0 is the initial electrical resistance in the unloaded state, ΔR is the electrical resistance change and P is applied pressure. For each experimental technique at least three measurements were performed in each sample.

Results and discussion

Morphological and FTIR characterisation.

The morphology of the samples and the dispersion of the CNT were evaluated by SEM, as shown in figure 2. Figure 2 shows the SEM images of SF/CNT composites with 0, 0.75 and 6 wt.% CNT content, being these images representative for the rest of the concentrations.

It is shown that the compact morphology of neat SF (figure 2a) is preserved in the composites (figure 2b-c). A good dispersion of CNT (bright spots in figure 2b-c) is observed for all the composites, independently of the filler content. Larger agglomerates were observed for the SF/CNT composites, with CNT clusters of ~1–2 µm in size, well distributed throughout the sample.

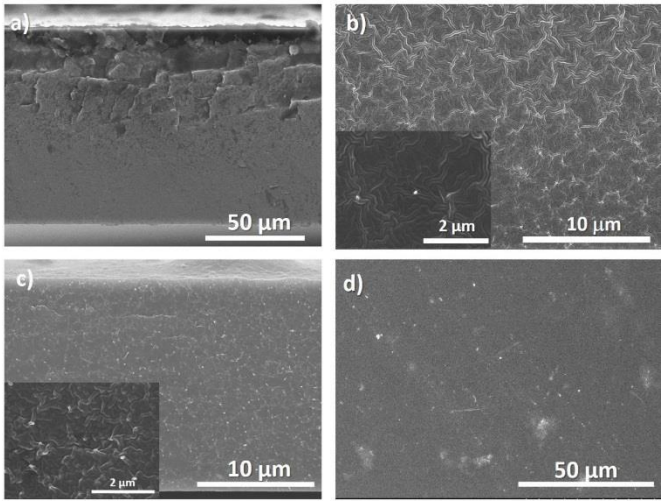

Figure 2. SEM cross-section images of SF/CNT composites of neat SF (a), 0.75 wt.% CNT (b) and 6 wt.% CNT (c) and surface image of 6wt.% CNT (d).

Figure 2c-d (6 wt.% CNT composite) shows that the fillers are also uniformly distributed along the cross-section of the samples, allowing suitable mechanical and electrical macroscopic response (see later). The insert in figure 2c also shows the proper wetting of the CNT by the polymer.

As it was observed by Zhou et al., SF films present globule-like nanostructure [32]. Films regenerated from formic acid solvent casting show globule-like size of around 100 nm [32] as consequence of SF chains self-assembling during solvent

evaporation process. SF/CNT composites show a similar structure for the different CNT concentrations.

In order to gain insight into the secondary structural changes of SF chains with the addition of the fillers, the ATR-FTIR spectra of the composites are presented in figure 3. Figure 3 shows the full-range ATR-FTIR spectra in which the frequency from 1800 cm^{-1} to 1400 cm^{-1} contains the most important amide I and amide II regions, describing the metastable state between a partially ordered α-helix and the β-sheet structures, and antiparallel β-sheet structure, respectively [33, 34].

The strong absorption at 3500–3000 cm^{-1} in figure 3a) represents the OH stretching vibration, H-bonded and NH stretching vibration [35].

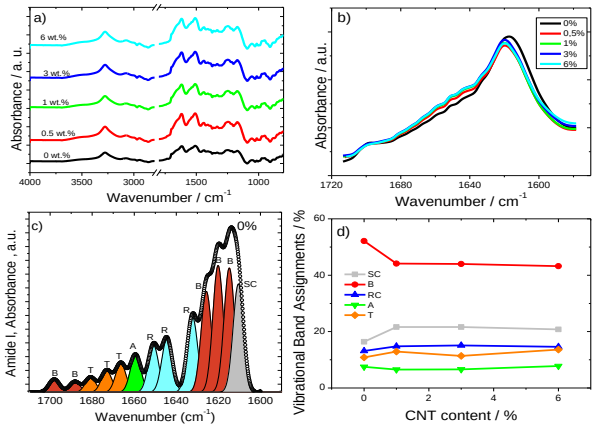

Figure 3. a) Full-range ATR-FTIR spectra for neat SF and the different composites. b) Amide I region of the ATR-FTIR spectra for all SF/CNT composites. c) Typical deconvolution spectrum of amide I for neat SF and d) Integral area fraction of the different spectral components resolved in this spectral region. The different contributions to the amide I envelope are marked as random coil (R, blue), β-sheets (B, red), α-helices (A, green), turns (T, orange), and side chains (SC, grey).

The secondary structures of SF are usually determined after the amide I band between 1700 to 1600 cm^{-1} (figure 2b) associated the C=O stretching vibration, NH in plane bending, out of phase CN stretching vibration, and CCN deformation [36]. Figure 2b) shows that the inclusion of CNT affects the vibration bands of SF but that the effect is independent of CNT content.

Amide I signals correspond to the vibration of different secondary protein structures such as side chains (1605–1615 cm^{-1}), β-sheets (1619–1628 and 1697–1703 cm^{-1}), random coil (1638–1655 cm^{-1}), α-helix (1656–1662 cm^{-1}), and turns (1663–1696 cm^{-1}) [37-39]. Thus, they can be differentiating, as figure 3c shows in a typical deconvolution indicating the corresponding area for each component for pure SF. The same procedure was performed for all SF/CNT composites and the results are summarized in figure 3d.

Figure 3d shows that the dominant conformation of SF is the β-sheet with 52%. This conformation is reduced to 44% for the SF/CNT composites independently of CNT content [36]. This, can be ascribed to a reduction on the degree of crystallinity of the samples [36], which is mainly attributed to the defects induced by the nanofillers as well as to noncovalent interactions between nanocarbon materials and silk fibroin through physisorption [40].

Figure 3d reveals that the proportion of the random coil and turns is practically the same (15 vs 13%, respectively) and the α-helix conformation is approximately 7% for all SF/CNT composites. Thus, the presence of the fillers does not modify those SF conformations.

Thermal and mechanical characterisation

The thermal and mechanical characterization of SF/CNT composites was performed to evaluate their dependence on CNT content, due to the thermal conductive properties and mechanical reinforcement effect of CNT [41].

DSC thermograms of the SF/CNT composites shown in figure 4a) demonstrate that all samples exhibit a similar thermal behaviour characterized by an endothermic peak around 290 °C associated with the degradation of SF molecular chains. Melting endotherm peaks were not observed in any samples because silk fibroin degrades at a temperature lower than the melting point.

During the heating scan an endothermic peak at 100 °C attributable to evaporation of bonded and non-bonded water was observed (Figure 4a) [42]. Some signals related to the loss of water show the ability of the samples to absorb ambient water during the casting process.

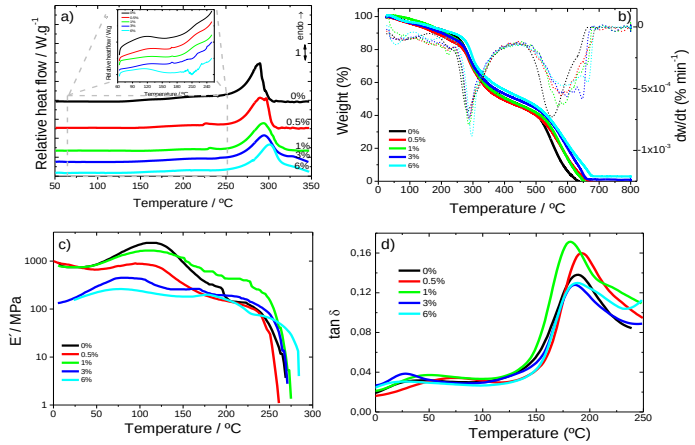

Figure 4. (a) DSC curves in the heating scan; (b) TGA thermograms; (c) viscoelastic modulus (E') and (d) loss tangent (tan δ) for SF and the corresponding SF/CNT composites

During the DSC heating scans, no relevant variations in the glass transition or random coil/α-helix to β sheet conformational changes were observed [43]. This behaviour usually observed in high crystalline samples corroborates FTIR data. Thermal degradation endothermic peak was not influenced by fillers addition, thus CNT-SF interactions not influence chains packing and their degradation.

TGA thermograms are essential for the determination of the temperature range in which the samples will not undergo any weight loss process affecting the macroscopic response of the materials. Further, it will allow to evaluate water content in the samples since SF has the ability to contain water molecules as shown in figure 4b [42].

Figure 4b) shows the TGA thermogram for all SF and SF/CNT samples, demonstrating that the decomposition of the samples occurs in two main stages.

An initial weight decrease is observed up to 150 °C for all samples (figure 4b) due to water removal (evaporation),

corresponding with the first DTGA peak. The storage of water in silk films can be of two different types: free water molecules that can be easily removed and, therefore, being the first to evaporate under heating and bonded-water, bonded to protein chains by the interactions between the amide groups of proteins and the OH groups of water [42].

The water content of the silk samples was determined by the weight decrease in the first step (figure 4b) and show a similar water content of ~10 % in all the samples, since CNTs do not vary the ability of silk fibroin to stock water.

The second degradation step ranges from 200 °C to 270 °C and corresponds to the degradation of the samples through the breakage of the primary chain of the silk molecules. This step is independent of the water content [42] and the inclusion of the CNT.

Before the second degradation peak in the DTG curve (figure 4b) a small peak at 235 °C is observed corresponding to a degradation of the less stable crystal domains not observed in pure SF samples.

The mechanical properties of the films, i.e, the elastic modulus (E') and the loss tangent (tan δ), are shown as a function of temperature (0 - 280 °C) at 1 Hz in figures 4c-d).

For all SF and SF/CNT composites (figure 4c) the elastic modulus remains constant until 50 ºC, sharply increases at about 100 ºC and then decreases abruptly at about 150 °C. This behaviour predicts water molecules plasticising effect over SF and make sense to the storage modulus increase as consequence of evaporation. With increasing temperature above 150 °C, the storage modulus decreases until reaching 280 °C where modulus strongly drops as a consequence of the beginning of the polymeric structure degradation, as shown in the TGA thermograms (figure 4b).

The loss tangent (figure 4d) increases slowly up to about 150 °C, increases sharply above this temperature, until it reaches a peak at about 180 °C.

The decrease in the elastic modulus (figure 4c) at about 150 °C and the peak of loss tangent (figure 4d) at 200 °C are explained in terms of the segmental motion of the main chains of the silk fibroin molecules in the amorphous film [44].

The storage modulus of the SF/CNT composites decreases with increasing CNTs content. Thus, the CNTs act as defects of the SF structure and, therefore, deteriorates the mechanical properties of the composites. This fact is particularly relevant for the SF/CNT composites with 6 wt.% filler content where the storage modulus decreases by two orders of magnitude when compared to the samples with the lowest CNTs content (figure 4c).

The CNTs content of 0.5 and 1 wt.% in SF/CNT composites is not enough to produce a significant mechanical variation and shows a similar behaviour to neat SF.

In addition, a slight destabilization of the glass temperature transition (Tg) is observed as indicated by the shift of the peak of tan δ (figure 4d) around 170- 180 °C, which slightly shifts to lower temperatures with increasing carbon nanotube content.

Electrical and electro-mechanical behaviour

For sensors applications, the electrical properties can be tuned by the inclusion of CNTs. The dielectric response (ε', tan δ and σ') calculated after equations 1 and 2 for the different samples is shown in figure 5.

Figures 5a) and b) show the dielectric constant and loss tangent, respectively, for SF and SF/CNTs composites, except for the composite with 6 wt.%, which is very conductive, as a function of the frequency at room temperature. For all samples, figure 5 a) and b) show that the dielectric constant and tan δ decreases as the frequency increases due to slow dipole mobility [45]. It is also detected that the dielectric constant increases with the addition of the CNTs, regardless of the frequency, due to increased charge carriers, with eventual contributions from the Maxwell-Wagner-Sillars (MWS) effect due to interfacial charge accumulation under an external electric field(figure 5a) [46]. This is also confirmed by the increase of both tan δ and σ' and shown in figures 5b and c.

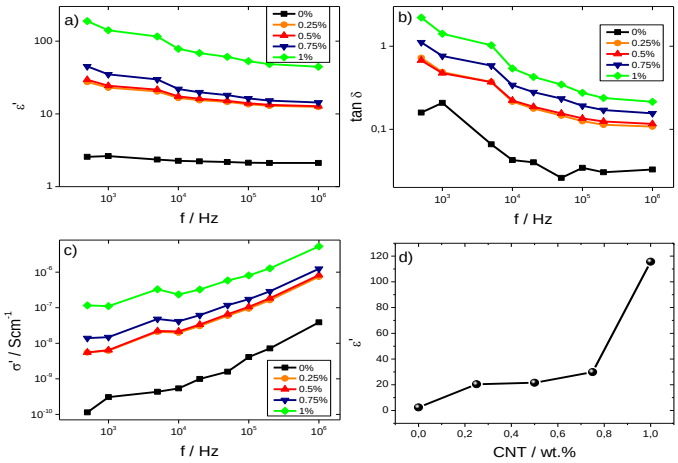

Figure 5. (a) dielectric constant, ε', (b) tan δ and (c) a.c. conductivity for all SF/CNTs composites. (d) Variation of the dielectric constant as a function of CNTs content at 5 kHz.

Figure 5(c) shows the σ' values for the different samples as a function of frequency. It is verified that the electrical conductivity increases with increasing frequency at room temperature, independently of the CNT content, indicating increased charge carrier mobility at localized states. The a.c conductivity increases with addition of CNTs due to both, the introduction of additional charge carriers and to the formation of a conductive network, until reaching a percolation, as shown in figure 6 for the d.c. conductivity [47-49].

Figure 5d) shows the room temperature dielectric constant of the samples at 5 kHz as a function of CNT content. The dielectric constant increases with increasing CNTs content due to contributions of the localized charge movement and the formation of local microcapacitors, as explained the percolation theory [50].

In order to determine the percolation threshold, the dc electrical conductivity was evaluated and the results as a function of CNT content are shown in figure 6.

The D.C. electrical conductivity increases by over 14 orders of magnitude when the filler content increased up to 6 wt.%, the percolation threshold being at approximately 1 wt.% of CNT.

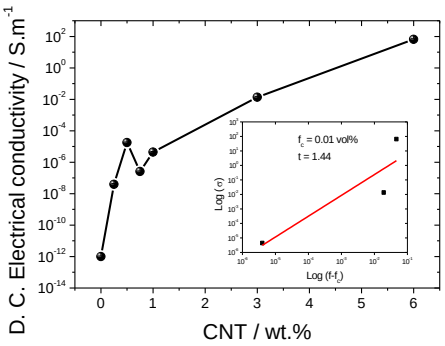

Figure 6. D.C. electrical conductivity of SF and the SF/CNT composites

The result of figure 6 show that the carbon nanotubes conductive networks is formed within the silk fibroin polymer. The electrical conductivity of SF/CNT composites can be theoretically predicted by the percolation model through the following equation [51]:

$$\sigma \approx (f - f_c)^t \text{ for } f > f_c \quad (5)$$

where f and f_c are the volume fraction of CNT and the percolation threshold of the SF/CNT composites, respectively, and t is the critical exponent in the conducting region.

It can be seen in the insert of figure 6, after the application of equation 5, that the percolation volume is f_c = 0.01 vol% (1 wt.%) and the critical exponent in the conducting region is t = 1.44. It is to notice that the critical exponent obtained for SF/CNT composites is 1.44, close to 1.1-1.3 for two-dimensional system [52].

Taking into account the electrical results of figure 6, the electromechanical performance was evaluated for SF/CNT composites with 1 and 3% wt.% of CNT, as shown in figure 6. It has been concluded that the piezoresistive response of carbonaceous composites is the largest around the percolation threshold due to larger variations of the conductive network under mechanical solicitation [22].

The electromechanical response was evaluated under compressive loading cycles with a maximum applied pressure of 400 N (equivalent to 0.88 MPa), as shown in Figure 7.

The loading-unloading pressure cycles from 50 up to 400 N are presented in Figure 7a), for 10 cycles in each measurement. Figure 7b) shows the relative variation of resistance during cycle loading and pressure application variation at a strain rate of 1 mm.min^{-1} for SF/CNT composites with 1 wt.% of CNT. The behavior is similar for the sample with 3 wt.% filler content.

It is observed that the piezoresistive behaviour presents an excellent response with small hysteresis effect (figure 7b and c). The stability of the cyclic response is shown in figure 7c by the resistance variation for 50 cycles. The minimum and maximum electrical resistance is constant with cycles (except for the initial 6-8 cycles), thus, we can conclude that the mechanical stability of these composites is good and can be used as sensor material.

It can be seen that SF/CNT composites present good reproducibility and signal stability and that the conductive network variations of carbon nanotubes into silk fibroin is stable, the resistance variations upon mechanical cycling being explained by variations of the tunnelling distance among fillers [53]. This fact is verified for both composites (1 and 3 wt.%).

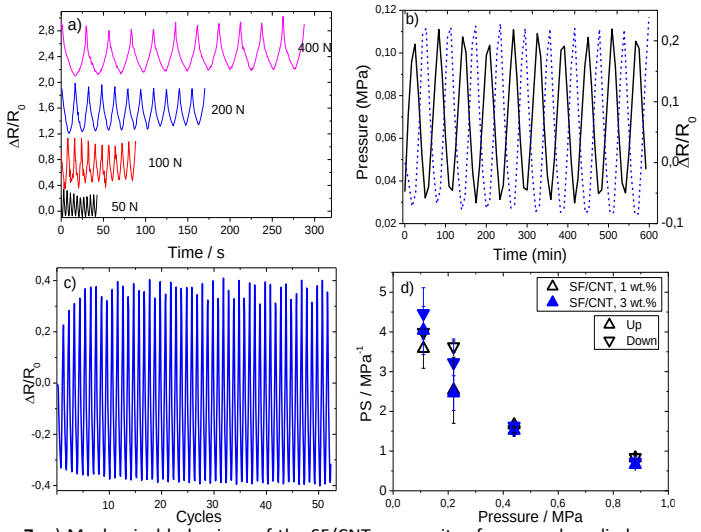

Figure 7. a) Mechanical behaviour of the SF/CNT composites for several applied forces (from 50 to 400 N). b) Pressure and relative resistance variation as a function of the time (up to 50 N or 0.11 MPa) for 1 wt.% of CNT and c) stability over repeated cycling (larger than 50 cycles) for the same sample. d) Piezoresistive performance in pressure sensibility (PS) up to pressures near 1 MPa for SF/CNT composites with 1 and 3 wt.% of CNT.

By applying varying maximum pressures (figure 7d) it is observed a decrease of the piezoresistive sensitivity (PS) upon increasing pressure: the application of increasing pressure leads to permanent reorientation and reconfiguration of the fillers and, eventually, conductive network breakage [31]. It is observed that the PS value is independent of CNT amount and it is the lowest (0.72 MPa^{-1}) for 0.88 MPa, due to the aforementioned permanent deformation of the conductive network.

The piezoresistive sensor based on silk fibroin shows excellent piezoresistive sensitivity value and represents an advance in comparison with the ones shown in the state-of-art for conventional polymers (i.e, thermoplastic polyurethane (TPU) [54, 55], polyester-based TPU [56], silicon rubber [57] and polydimethylsiloxane (PDMS) [58]) in terms of environmental friendliness.

Implementation of a pressure sensor prototype based on SF/CNT composites

As a proof of concept of the suitability of the materials for sensor applications, a simple prototype was fabricated envisioning that it could be used as a touch/pressure sensor, for example, by being embedded inside the paper sheets of a hybrid book, allowing a digital interaction with the user, but without the negative environmental impact that plastic-based sensors usually carry on. Therefore, the developed silk-based material can be used as a touch/pressure sensor, either analogically or digitally.

To achieve that goal, two pairs of gold electrodes were deposited in the film using sputtering technique, two in the top layer and the other two in the bottom layer, so that each pair was overlapping, as presented in Figure 8a). A SF/CNT film with 1 wt.% CNT content was used due to its s electrical resistivity: >> 200 MΩ between side electrodes, and 150 to 300 kΩ approximately between top and bottom pairs. Therefore, if multiple pressure points are being evaluated simultaneously, no interference will occur between a pair of sensing elements within one film.

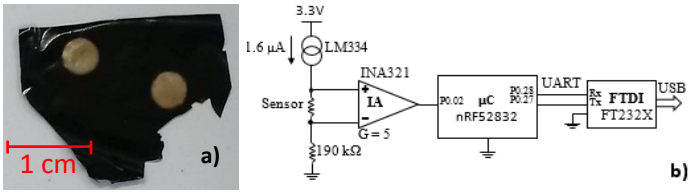

Figure 8 – a) SF/CNT 1 wt.% CNT content film with 4 gold electrodes (2 on top and 2 on bottom); b) Schematic of the test circuit, consisting in a current source and an instrumentation amplifier (IA).

Two terminals were connected per electrode to assure the good electrical connection between the terminals and the electrodes, which consisted in aluminium foil glued to the electrodes with z-axis conductive adhesive tape (3M 9703). The maximum terminal-electrode-terminal resistance measured in the prototype was < 100 Ω, which warranted a good connection from the terminals to the electrodes.

The developed circuit to measure sensor response was based on a current source through the sensor, shown in Figure 8b), which provides a linear voltage drop on the sensor versus its resistance, which can be amplified by an instrumentation amplifier (IA), and then fed to the analog-to-digital converter (ADC) of a microcontroller (µC). Finally, the data is sent to a computer via a Universal Serial Bus (USB) to universal asynchronous receiver-transmitter (UART) converter.

The selected components for the circuit were as follows: current source: Texas Instruments LM334; IA: Texas Instruments INA321; µC: Nordic Semiconductor nRF52832; USB to UART converter: FTDI Chip FT232X.

The IA is characterized by a gain (G) of 5, which amplifies the differential voltage in the sensor to 1.2 V to 2.4 V. The 190 kΩ resistance in the negative pin of the IA simply rises the voltage in this pin to 304 mV, above the minimum operating voltage of the IA. The reference voltage for the ADC comparison was 3.3 V. The sensor was read at a rate of 100 samples per second, using 8 bits, and the UART communication was configured with a baud rate of 1 Mbps.

Figure 9 shows that the resistance variation of SF/CNT composites when the pressure is applied by a fingertip touch. The resistance response is proportional to the deformation (Figure 7 and Figure 9) and recovers the initial values when the pressure is released.

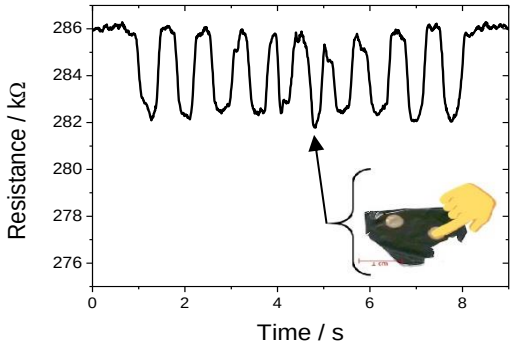

Figure 9 - Resistance variation response when force was applied on the sensor by a fingertip touch.

Thus, considering environmental issues and the suitable electro-mechanical response of the developed SF/CNT composites, the present work demonstrates the applicability of these natural polymer based composites for the development of the next generation of multifunctional pressure and deformation sensors.

Conclusions

Silk fibroin/carbon nanotube SF/CNT composites have been prepared for pressure sensor applications. The composites were prepared by solvent-casting method with different filler contents (0-6 wt.%). The CNT fillers were homogeneously distributed in the silk fibroin matrix and the thermal and mechanical properties of these composites are independent of the CNT content.

The addition of CNT into the silk fibroin matrix affects the β sheet content and the electrical properties (dielectric constant and electrical conductivity). The content of the β sheet decreases and the electrical conductivity increases with increasing CNT content.

The composites show a significant increase of the electrical conductivity with increasing filler content, the percolation threshold being around 3wt.% of CNT.

The piezoresistive behaviour of these composites shows a correspondence with the applied pressure without hysteresis.

In addition, the electro-mechanical behaviour shows good reproducibility over cyclic loading and suitable pressure sensitivity of ~ 4 MPa^{-1} at small pressures of 0.11 MPa. The results were confirmed by the implementation of a touch/pressure sensor prototype with the corresponding readout electronics.

Thus, it is concluded that the SF/CNT composites show excellent overall performance to contribute to the development of high-performance pressure sensors based on natural polymers.

Conflicts of interest

There are no conflicts to declare.

Acknowledgements

The authors thank the FCT (Fundação para a Ciência e Tecnologia) for financial support under the framework of Strategic Funding grants UID/FIS/04650/2013, UID/EEA/04436/2013 and UID/QUI/0686/2016; and project no. PTDC/FIS-MAC/28157/2017. The authors also thank the FCT for financial support under grants SFRH/BD/110622/2015 (S.G.), SFRH/BPD/112547/2015 (C.M.C.) and SFRH/BPD/110914/2015 (P.C.). Financial support from the Spanish Ministry of Economy and Competitiveness (MINECO) through project MAT2016-76039-C4-3-R (AEI/FEDER, UE) (including FEDER financial support) and from the Basque Government Industry and Education Departments under the ELKARTEK, HAZITEK and PIBA (PIBA-2018-06) programs, respectively, is also acknowledged

Notes and references

1. S. Kalia, B. S. Kaith and I. Kaur, *Polymer Engineering & Science*, 2009, **49**, 1253-1272.
2. M. T. Sebastian and H. Jantunen, *International Journal of Applied Ceramic Technology*, 2010, **7**, 415-434.
3. Y. Yu, B. Zhang, M. Feng, G. Qi, F. Tian, Q. Feng, J. Yang and S. Wang, *Composites Science and Technology*, 2017, **147**, 62-70.
4. D. Ayre, *Current Opinion in Green and Sustainable Chemistry*, 2018, **13**, 108-112.
5. M. G. A. Vieira, M. A. da Silva, L. O. dos Santos and M. M. Beppu, *European Polymer Journal*, 2011, **47**, 254-263.
6. M. Niaounakis, *Biopolymers: Applications and Trends*, Elsevier Science, 2015.
7. L.-D. Koh, Y. Cheng, C.-P. Teng, Y.-W. Khin, X.-J. Loh, S.-Y. Tee, M. Low, E. Ye, H.-D. Yu, Y.-W. Zhang and M.-Y. Han, *Progress in Polymer Science*, 2015, **46**, 86-110.
8. R. F. P. Pereira, M. M. Silva and V. de Zea Bermudez, *Macromolecular Materials and Engineering*, 2015, **300**, 1171-1198.
9. H. Zhang, J. Magoshi, M. Becker, J. Y. Chen and R. Matsunaga, *Journal of Applied Polymer Science*, 2002, **86**, 1817-1820.
10. Y. Cheng, L.-D. Koh, D. Li, B. Ji, M.-Y. Han and Y.-W. Zhang, *Journal of The Royal Society Interface*, 2014, **11**.
11. D. N. Rockwood, R. C. Preda, T. Yücel, X. Wang, M. L. Lovett and D. L. Kaplan, *Nature Protocols*, 2011, **6**, 1612.
12. C. Jiang, X. Wang, R. Gunawidjaja, Y.-H. Lin, M. K. Gupta, D. L. Kaplan, R. R. Naik and V. V. Tsukruk, *Advanced Functional Materials*, 2007, **17**, 2229-2237.
13. Y. Qi, H. Wang, K. Wei, Y. Yang, R.-Y. Zheng, I. Kim and K.-Q. Zhang, *International Journal of Molecular Sciences*, 2017, **18**, 237.
14. L.-D. Koh, J. Yeo, Y. Y. Lee, Q. Ong, M. Han and B. C. K. Tee, *Materials Science and Engineering: C*, 2018, **86**, 151-172.
15. D.-H. Kim, J. Viventi, J. J. Amsden, J. Xiao, L. Vigeland, Y.-S. Kim, J. A. Blanco, B. Panilaitis, E. S. Frechette, D. Contreras, D. L. Kaplan, F. G. Omenetto, Y. Huang, K.-C. Hwang, M. R. Zakin, B. Litt and J. A. Rogers, *Nature Materials*, 2010, **9**, 511.
16. P. Vadgama, in *Encyclopedia of Materials: Science and Technology*, eds. K. H. J. Buschow, R. W. Cahn, M. C. Flemings, B. Ilschner, E. J. Kramer, S. Mahajan and P. Veyssière, Elsevier, Oxford, 2001, DOI: https://doi.org/10.1016/B0-08-043152-6/00113-3, pp. 592-595.
17. J. Oliveira, V. Correia, H. Castro, P. Martins and S. Lanceros-Mendez, *Additive Manufacturing*, 2018, **21**, 269-283.
18. S. Stassi, V. Cauda, G. Canavese and C. Pirri, *Sensors*, 2014, **14**, 5296.
19. D. Prasad, L. Zhiling, N. Satish and E. V. Barrera, *Nanotechnology*, 2004, **15**, 379.
20. K. P. Sau, T. K. Chaki and D. Khastgir, *Composites Part A: Applied Science and Manufacturing*, 1998, **29**, 363-370.
21. A. Ferreira, P. Cardoso, D. Klosterman, J. A. Covas, F. W. J. v. Hattum, F. Vaz and S. Lanceros-Mendez, *Smart Materials and Structures*, 2012, **21**, 075008.
22. A. Ferreira and S. Lanceros-Mendez, *Composites Part B: Engineering*, 2016, **96**, 242-247.
23. P. Costa, J. Nunes-Pereira, J. Oliveira, J. Silva, J. A. Moreira, S. A. C. Carabineiro, J. G. Buijnsters and S. Lanceros-Mendez, *Composites Science and Technology*, 2017, **153**, 241-252.
24. S. Cravanzola, G. Haznedar, D. Scarano, A. Zecchina and F. Cesano, *Carbon*, 2013, **62**, 270-277.
25. A. Ferrreira, J. G. Rocha, A. Ansón-Casaos, M. T. Martínez, F. Vaz and S. Lanceros-Mendez, *Sensors and Actuators A: Physical*, 2012, **178**, 10-16.
26. P. Costa, S. Ribeiro and S. Lanceros-Mendez, *Composites Science and Technology*, 2015, **109**, 1-5.
27. C. Dionigi, T. Posati, V. Benfenati, A. Sagnella, A. Pistone, S. Bonetti, G. Ruani, F. Dinelli, G. Padeletti, R. Zamboni and M. Muccini, *Journal of Materials Chemistry B*, 2014, **2**, 1424-1431.
28. M. Kang, P. Chen and H.-J. Jin, *Current Applied Physics*, 2009, **9**, S95-S97.
29. P. Tseng, G. Perotto, B. Napier, P. Riahi, W. Li, E. Shirman, D. L. Kaplan, I. V. Zenyuk and F. G. Omenetto, *Advanced Electronic Materials*, 2016, **2**, 1600190.
30. S. M. Kwon, H. S. Kim and H. J. Jin, *Advanced Materials Research*, 2008, **47-50**, 1105-1108.
31. H. Zhao and J. Bai, *ACS Applied Materials & Interfaces*, 2015, **7**, 9652-9659.
32. J. Zhou, B. Zhang, L. Shi, J. Zhong, J. Zhu, J. Yan, P. Wang, C. Cao and D. He, *ACS Applied Materials & Interfaces*, 2014, **6**, 21813-21821.
33. S. Ling, Z. Qi, D. P. Knight, Z. Shao and X. Chen, *Polymer Chemistry*, 2013, **4**, 5401-5406.
34. J. Zhong, M. Ma, W. Li, J. Zhou, Z. Yan and D. He, *Biopolymers*, 2014, **101**, 1181-1192.
35. W. Qiu, W. Teng, J. Cappello and X. Wu, *Biomacromolecules*, 2009, **10**, 602-608.
36. O. S. Rabotyagova, P. Cebe and D. L. Kaplan, *Macromolecular Bioscience*, 2010, **10**, 49-59.
37. O. N. Tretinnikov and Y. Tamada, *Langmuir*, 2001, **17**, 7406-7413.
38. X. Hu, D. Kaplan and P. Cebe, *Macromolecules*, 2006, **39**, 6161-6170.
39. B. D. Lawrence, F. Omenetto, K. Chui and D. L. Kaplan, *Journal of Materials Science*, 2008, **43**, 6967.
40. Q. Wang, C. Wang, M. Zhang, M. Jian and Y. Zhang, *Nano Letters*, 2016, **16**, 6695-6700.
41. R. Andrews and M. C. Weisenberger, *Current Opinion in Solid State and Materials Science*, 2004, **8**, 31-37.
42. K. Yazawa, K. Ishida, H. Masunaga, T. Hikima and K. Numata, *Biomacromolecules*, 2016, **17**, 1057-1066.

43. N. Agarwal, D. A. Hoagland and R. J. Farris, *Journal of Applied Polymer Science*, 1997, **63**, 401-410.
44. T. Yucel, P. Cebe and D. L. Kaplan, *Advanced functional materials*, 2011, **21**, 779-785.
45. F. Kremer and A. Schönhals, *Broadband Dielectric Spectroscopy*, Springer Berlin Heidelberg, 2012.
46. S. Song, S. Xia, S. Jiang, X. Lv, S. Sun and Q. Li, *Materials*, 2018, **11**, 347.
47. H. S. Dahiya, N. Kishore and R. M. Mehra, *Journal of Applied Polymer Science*, 2007, **106**, 2101-2110.
48. Lin Zhang, Patrick Bass and Z.-Y. Cheng, *Applied Physics Letters*, 2014, **105**, 042905.
49. C. Liu, L. Zheng, L. Yuan, Q. Guan, A. Gu and G. Liang, *The Journal of Physical Chemistry C*, 2016, **120**, 28875-28885.
50. C.-W. Nan, Y. Shen and J. Ma, *Annual Review of Materials Research*, 2010, **40**, 131-151.
51. F. He, S. Lau, H. L. Chan and J. Fan, *Advanced Materials*, 2009, **21**, 710-715.
52. J.-F. Gao, Z.-M. Li, Q.-j. Meng and Q. Yang, *Materials Letters*, 2008, **62**, 3530-3532.
53. N. Hu, Y. Karube, C. Yan, Z. Masuda and H. Fukunaga, *Acta Materialia*, 2008, **56**, 2929-2936.
54. H. Liu, Y. Li, K. Dai, G. Zheng, C. Liu, C. Shen, X. Yan, J. Guo and Z. Guo, *Journal of Materials Chemistry C*, 2016, **4**, 157-166.
55. H. Liu, M. Dong, W. Huang, J. Gao, K. Dai, J. Guo, G. Zheng, C. Liu, C. Shen and Z. Guo, *Journal of Materials Chemistry C*, 2017, **5**, 73-83.
56. L. Lin, H. Deng, X. Gao, S. Zhang, E. Bilotti, T. Peijs and Q. Fu, *Polymer International*, 2013, **62**, 134-140.
57. W. Luheng, D. Tianhuai and W. Peng, *Carbon*, 2009, **47**, 3151-3157.
58. J. Hwang, J. Jang, K. Hong, K. N. Kim, J. H. Han, K. Shin and C. E. Park, *Carbon*, 2011, **49**, 106-110.